Research Article | Vol. 33, No. 2 / 27 Jan 2025 / Optics Express 2512
Optics EXPRESS

Optical tactile sensor based on a flexible optical fiber ring resonator for intelligent braille recognition

HENG WANG,[1] LIN MA,[1] QIN NIE,[1] XUEHAO HU,[2] XIAOLI LI,[3,4] RUI MIN,[3,4] AND ZHUO WANG[5,*]

[1]College of Science, Shenyang Aerospace University, Shenyang 110136, China
[2]Department of Electromagnetism and Telecommunication, University of Mons, 7000 Mons, Belgium
[3]Department of Psychology, Faculty of Arts and Sciences, Beijing Normal University, Zhuhai 519087, China
[4]Faculty of Psychology, Beijing Normal University, Beijing 100875, China
[5]Department of Physics, Faculty of Arts and Sciences, Beijing Normal University, Zhuhai 519087, China
*zhuowang@bnu.edu.cn

Abstract: Inspired by human skin, bionic tactile sensing is effectively promoting development and innovation in many fields with its flexible and efficient perception capabilities. Optical fiber, with its ability to perceive and transmit information and its flexible characteristics, is considered a promising solution in the field of tactile bionics. In this work, one optical fiber tactile sensing system based on a flexible PDMS-embedded optical fiber ring resonator (FRR) is designed for braille recognition, and the Pound-Drever-Hall (PDH) demodulation scheme is adopted to improve the detection sensitivity. Theoretical simulations and experimental verifications show that by adopting a bionic sliding approach and a Multilayer Perceptron Neural Network, a single FRR with a hardness gradient design can detect eight different tactile pressures in braille characters with an accuracy of 98.57%. Furthermore, after training and testing, the MLP-LSTM model classifies time series signals, thereby achieving completely accurate encoding of braille keywords and braille poems. The advantages of the optical fiber tactile sensing system in this study are that the high-quality factor FRR can detect subtle differences in braille dots, it is not affected by changes in optical power due to its relies on PDH frequency demodulation, and the application of machine learning algorithms can enhance the robustness to slight pressure errors and simplify the recognition process. This solution opens up what we believe is a new optical approach for bionic tactile perception and has important potential value in promoting human-computer interaction, smart medical care, and other fields.

1. Introduction

The human tactile perception system is a complex network of specialized cells, nerves, and brain regions that allow us to feel and perceive the world around us. It plays a crucial role in everyday activities, from picking up delicate objects to navigating our environment in the dark [1]. Tactile sensing encompasses many critical applications, including intelligent robots, biomimetic prosthetics, remote surgery, and human-machine interfaces (HMI) [2–4]. Tactile pressure sensors are crucial components of intelligent robots. Detecting pressure is particularly important as it enables robots to perceive, grasp, and hold objects, and increasing the sensitivity of these sensors enhances their performance in these tasks [5,6]. Moreover, the biological haptic perception of the human fingertip involves identifying and recognizing objects and surface textures, which requires high spatial resolution in sensor structures and fast response to subtly changing dynamic pressure [7,8]. In the fields of life health and auxiliary medicine, tactile perception also plays

#546873 https://doi.org/10.1364/OE.546873
Journal © 2025 Received 1 Nov 2024; revised 1 Dec 2024; accepted 2 Dec 2024; published 16 Jan 2025

Optics EXPRESS

an important role. The emergence of bionic skin has effectively improved the quality of life of patients with burns and scalds.

In addition to the above situations, the importance of tactile sense to the blind cannot be ignored. According to the World Health Organization's (WHO) most recent data, at least 2.2 billion people globally have vision impairment. These individuals face challenges on daily activities and social interactions due to impaired visual function, which has become a significant public and social concern in contemporary society. Invented by Louis Braille in 1824, braille is an effective tool for blind and visually impaired people to acquire information by touching printed dots on a braille board with their fingers [9]. However, learning and reading braille can be challenging, prompting researchers to develop effective technology to assist blind individuals.

There are two main approaches to braille recognition. One common approach is to acquire and preprocess braille images, and then extract information by analyzing the image features with computer algorithms. However, due to device limitations and the small size of braille characters, the vision-based scheme using image processing faces several challenges, including susceptibility to variations in ambient light and images taken from different distances and angles [10,11]. As an alternative scheme to acquire information about braille, the tactile sensing technique exhibits excellent performance while avoiding the aforementioned constraints and is expected to be an effective way to realize braille recognition. Electric tactile sensors are typically based on piezoresistance [12], piezoelectric [13], capacitive [10], and laser-induced graphene (LIG) [14] enabling the detection of subtle changes on touch surfaces. When a user touches the sensor surface with their finger, the sensor can detect the position and pressure of the contact point, subsequently converting this information into electrical signals. These signals, after processing, can be used to identify the braille characters being touched. Optical tactile sensors also hold significant potential in braille recognition, as these sensors detect changes in light to perceive touch position, pressure, and shape, thereby enabling the recognition of braille characters. Their operating principles often involve the reflection, refraction, or scattering of light. The main types of optical tactile sensors include micro-nano optical fiber sensors [15] and FBG sensors [16]. When combined with machine learning or pattern recognition techniques, these sensors can achieve automated braille recognition, converting physical tactile inputs into speech or text outputs, thus aiding visually impaired individuals in reading and accessing information more conveniently. Optical tactile sensors exhibit clear advantages in terms of precision, interference resistance, flexibility, and integration potential, particularly in complex environments or applications that demand high precision in braille recognition [17–19]. However, factors such as tactile detection sensitivity and environmental disturbances have always restricted the development of optical tactile sensors, making them less suitable for the recognition of smaller braille dots.

In view of the advantages of optical sensors in tactile perception, this study proposes a method for braille recognition that combines high-precision fiber optic sensing methods with AI algorithms. The FRR has the advantages of simple preparation, flexible design, and high-quality factor, which is consistent with the material and sensitivity requirements needed as a bionic material. Here, one optical fiber tactile sensing system is reported, which utilizes a FRR as the sensor and employs the Pound-Drever-Hall (PDH) scheme for demodulation [20–23]. The FRR is encapsulated with PDMS to form an optical skin, and protrusions of different hardness are fixed on it to achieve effective recognition of different braille dot tactile pressure. The PDH interrogation signal is then used for braille recognition with the help of the MLP-LSTM machine learning algorithm. The advantage of combining PDH technology with machine learning algorithms to achieve braille recognition is that the high-quality factor resonator can distinguish the tiny pressure signals of braille dots, effectively improving the signal detection resolution, and the machine learning algorithm further improves the robustness and dynamics of the system, avoiding pressure errors caused by environmental factors. It not only realizes the efficient recognition and

Optics EXPRESS

intelligent transcoding of braille information, but also has significant potential application value in fields such as human-computer interaction and intelligent manufacturing.

2. Bionic optical fiber tactile sensing system

The biological tactile sensing system is an important condition for the survival of organisms. As shown in Fig. 1(a), human skin contains a variety of tactile sensors, which are then transmitted to the brain through the nervous system for information recognition and processing. Inspired by this principle, this study proposed a bionic tactile sensing system as shown in Fig. 1(b). An optical tactile bionic system for braille recognition is constructed, encompassing sensor structure design, optical fiber signal transmission, and AI algorithm-based information processing. The configuration of the optical fiber tactile sensing system for braille recognition is structured as follows in Fig. 2: A single-frequency tunable laser (NKT Photonics Koheras Basik E15) with a narrow linewidth (<0.1 kHz) serves as the light source for the sensory system. The laser is driven by a triangular wave to sweep within a narrow range, producing a series of resonant peaks directly detected through the intensity of the transmitted light. The laser phase is modulated by a phase modulator (PM, iXblue photonics $LiNbO_3$) driven by a sine wave signal $M \sin 2\pi f_m t$, resulting

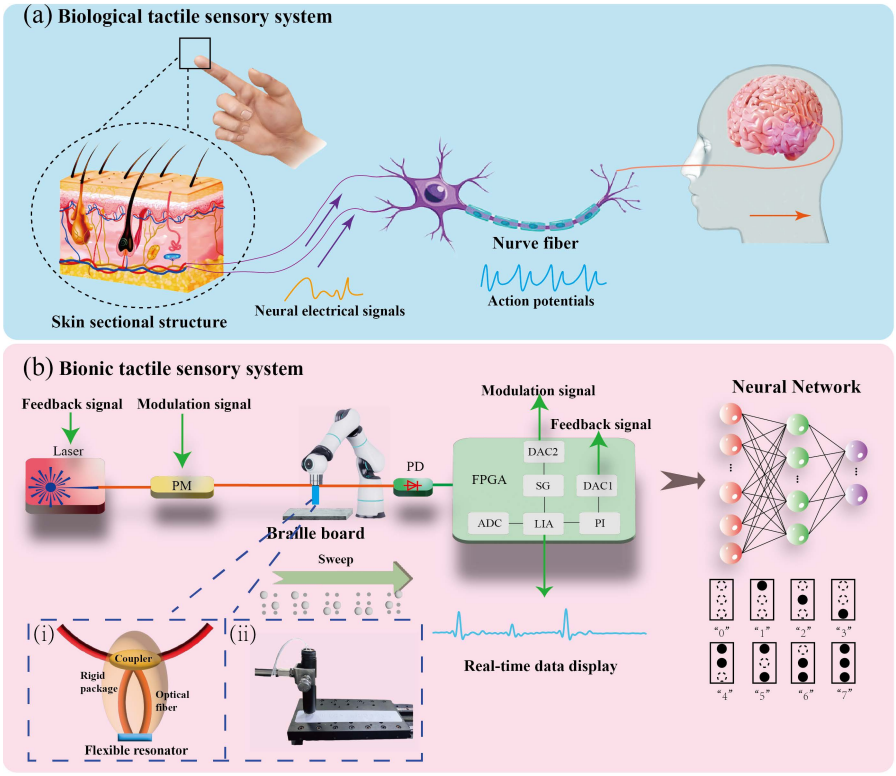

Fig. 1. (a)Schematic illustration of the biological tactile sensory system. (b) Schematic illustration of the bionic tactile sensory system. PM, electro-optic phase modulator; PD, photo-detector; ADC, analog-digital converter; DAC, digital-analog converter; SG, signal generator; LIA, lock-in amplifier; PI, proportional integral controller. (i) Schematic diagram of fiber optic resonator tactile sensor. The FRR is encapsulated with PDMS and rigid package, leaving only the sensing area (blue) exposed for braille recognition. (ii) Experimental diagram of optical fiber resonator tactile sensor. The encapsulated flexible sensor is fixed on the translation stage for braille recognition.

Optics EXPRESS

in the generation of carrier and high-order sideband components. The error signal (also called the PDH curve) is demodulated using a lock-in amplifier (LIA), with the detailed theoretical derivation provided in Appendix A. The PDH error signal is then split into two branches for frequency synchronization and analysis. One branch is sent to a proportional-integral (PI) servo controller, where the PI controller is activated, and the laser sweep is disabled. The error signal is fed to the piezoelectric transducer (PZT) to modulate the laser frequency, enabling the closed-loop system to synchronize the laser frequency with the cavity resonance frequency. The other branch is extracted for further analysis and serves as the system output.

When the FRR equipped with different gradient tactile pressure relief designs slides over the braille board, the pressure exerted by the raised braille dots causes slight changes in the length and refractive index of the optical fiber. These changes alter the phase of the light transmitted through the fiber, leading to a shift in the resonant frequency of the FRR. This frequency shift can be detected by the PDH system. As three raised dots can form eight different arrangements, the PDH system generates error signals corresponding to the pressure signals from these eight different arrangements. In practice, even for the same arrangement, there may be slight pressure differences when the FRR slides over the dots, resulting in signals that are not exactly identical. To address this, machine learning methods are employed to classify these signals using a large amount of experimental data. Through this processing and analysis, the corresponding arrangement of braille dots from the signals output by the PDH system is identified, thereby decoding the information conveyed by the braille.

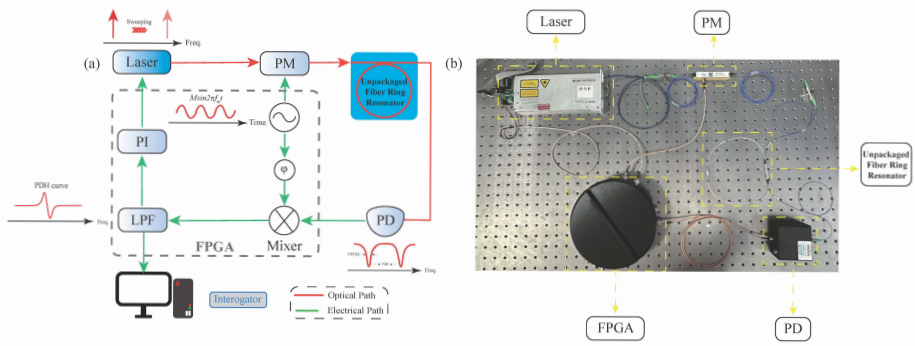

Fig. 2. Schematic configuration of the PDH system (a) and experimental setup (b). PM, electro-optic phase modulator; PD, photo-detector; LPF, low-pass filter; PI, proportional integral controller.

3. Theoretical analysis

3.1. Theoretical analysis of optical fiber tactile pressure sensing

External pressure applied to the FRR leads to resonance shifts due to the stress-strain and photo-elastic effects of the optical fiber. The stress-strain effect changes the length of the optical fiber, affecting the phase of the light wave traveling through it. Similarly, the photo-elastic effect impacts the refractive index of the optical fiber, also affecting the phase of the light wave. Under the influence of these combined effects, resonance shifts of the FRR ultimately occur.

The phase of light transmitted in an optical fiber changes when the fiber is subjected to stress and temperature from external sources. When pressure is applied to an optical fiber, elastic deformation, caused by the stress-strain effect, occurs, leading to a change in the fiber's length. Additionally, the photo-elastic effect alters the refractive index of the fiber core. Similarly, temperature variations modify the effective refractive index and length of the fiber, causing phase

Optics EXPRESS

changes. These changes result in a phase shift in the light wave propagating through the fiber [24]. The optical fiber has a thermo-optic coefficient of $1 \times 10^{-5}\ ^\circ\ C^{-1}$ and a coefficient of thermal expansion of $5.5 \times 10^{-6}\ ^\circ\ C^{-1}$. The braille recognition experiment is typically conducted at room temperature, where temperature variations have a negligible effect on the resonant frequency of the cavity compared to pressure-induced effects. The relationship between phase change and pressure and temperature variations can be expressed as:

$$\begin{aligned} \Delta\phi &= \Delta\phi_\sigma + \Delta\phi_T \\ &= a_\sigma \Delta P + a_T \Delta T \\ &\approx a_\sigma \Delta P \end{aligned} \tag{1}$$

where $\Delta\phi_\sigma$ and $\Delta\phi_T$ are the phase change of the light through the fiber caused by applied pressure and temperature, respectively. ΔP and ΔT are the change of applied pressure and temperature. a_σ and a_T are the coefficients related to applied pressure and temperature changes. According to the resonance condition (5), $\frac{n_{eff}L}{c}$ is related to the resonance frequency. So the resonance shift of the optical resonator is proportional to the phase change of the light wave propagating within the cavity [25], and this relationship can be expressed as:

$$\begin{aligned} \Delta\phi &= \frac{2\pi n_{eff} L}{c} \Delta f \\ &= \frac{2\pi q}{f_{res}} \Delta f \\ &= \frac{1}{b} \Delta f \end{aligned} \tag{2}$$

where n_{eff} is the effective refractive index of optical fiber, L is the length of resonator, c is the light speed, f_{res} is the resonance frequency, and Δf is the resonance shift of the resonator. According to Eq. (9), the voltage shift of the PDH error signal is proportional to the resonance shift. Therefore, the relationship between the voltage shift and the applied pressure can be concluded as follows:

$$\begin{aligned} \Delta P &= \frac{1}{k_0 b a_\sigma} \Delta V \\ &= K \Delta V \end{aligned} \tag{3}$$

where b is a constant denoting the sensitivity of the system.

3.2. Braille sensor parameters analysis and simulation

Before experimentation, performing simulations and analytical calculations is crucial to identify optimal experimental conditions. Figure 3(a) illustrates the overall sensing principle of the system. The resonant frequency of the FRR shifts in response to applied pressure, and this frequency shift is demodulated by the PDH system. The demodulated signal is then used as the system's output to measure the pressure. The quality factor (Q) is a critical parameter for the FRR, characterizing its ability to couple and confine intracavity photon energy. The Q value of the resonant cavity can be influenced by various factors, such as the coupling coefficient, transmission loss, light source coherence, and external disturbances. In this study, the coupling coefficient and transmission loss are considered, as the two factors have significant effects on the Q value and can be controlled in the experiment. The value of Q can be calculated by $Q = f_0/FWHM$, where f_0 represents the resonance frequency. In the simulation, the FRR was configured with the following parameters: an effective refractive index of the optical fiber of 1.45, a fiber length (L) of 2 meters, an initial laser wavelength of 1550 nm, and a laser linewidth of 100 Hz. Figure 3(b) presents the simulation results. This Q value directly indicates the detection sensitivity of the resonator. A high-Q

Optics EXPRESS

resonator is characterized by a narrower linewidth and exhibits a steeper slope of frequency discrimination sensitivity in the demodulation curve, allowing for the detection of larger signals even in response to minor resonant frequency shifts. According to the simulation results, the FRR was then constructed by connecting one input port and one output port of a commercial single-mode fiber 2×2 optic coupler. The coupling coefficient of the coupler was set to 0.1, and the length of the resonator fiber was 2 meters. The insertion loss of the coupler, measured using an optical power meter, was approximately 0.3 dB, while the connection loss was estimated to be around 0.2 dB.

According to Eq. (8), the PDH curve after demodulation by the LIA amplifier is linear near the resonance of the FRR and crosses the zero point when the laser output frequency is exactly at the resonant frequency of the FRR. The slope of the linear region dictates the frequency discrimination sensitivity of the resonator, and its linear response range is approximately equal to the Full Width at Half Maximum (FWHM). The PDH error signal exhibits dependence on various parameters, including the structural parameters of the resonator, modulation depth, and modulation frequency. Figure 3(c) shows the simulation of the change in the zero-point slope under varying modulation voltages and modulation frequencies. Furthermore, formulas (8) and (9) show that once the structural parameters of the resonator are fixed, the frequency discrimination slope is only related to the modulation frequency, modulation depth, and phase difference between the error signal and the reference signal. According to the theory of coherent detection, the phase difference is adjusted through the phase shifter, and when the phase difference is $\frac{\pi}{2}$, the lock-in amplifier obtains the maximum error signal. Therefore, the frequency discrimination slope mainly depends on the modulation frequency and depth.

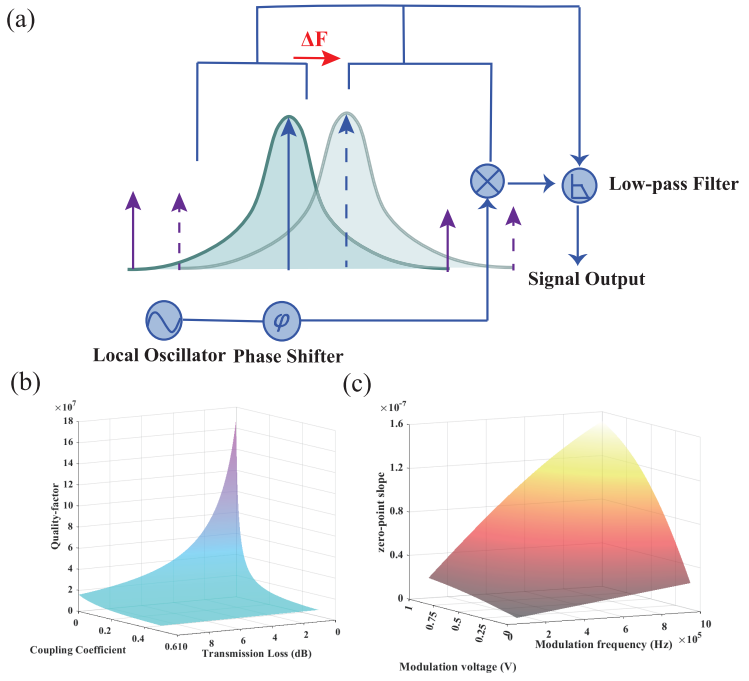

Fig. 3. Principle of demodulation using PDH. (b) Simulation results of Q influenced by coupling coefficient and transmission loss. (c) Simulation results of zero-point slope influenced by modulation frequency and modulation voltage.

Optics EXPRESS

4. Experiment

4.1. Fabrication of braille sensor

To differentiate between various braille arrangements in a single column (three rows and one column), we propose a novel sensor structure.As shown in Fig. 4 Step 1, a 3D-printed mold designed by solidworks was used for fiber packaging. Firstly, the PDMS precursor and curing agent were mixed at a ratio of 10:1, and the mixture was left at room temperature for 20 minutes to remove bubbles. The optical fiber was placed into the mold, the PDMS solution was injected into it, and the assembly was cured on a heating plate at 80°C for 20 minutes. Furthermore, PDMS was injected onto the packaged fiber surface to form three protrusions with different hardness levels, as the solutions were made by mixing different proportions. When the optical fiber slides over braille, the variations in the arrangement of braille dots cause distinct effects on the fiber due to material differences, with harder protrusions exerting more pronounced impacts. The positions of the protrusions in the sensing region align with the braille dots, with a spacing of approximately 2.5 mm. After demolding from the 3D-printed mold, the region surrounding the three protrusions is carefully trimmed into an approximately rectangular shape. The exact dimensions of the rectangular are not strictly specified, as long as it fully encompasses the three protrusions and is kept as small as possible to facilitate the subsequent packaging of the FRR. The core component of the sensor is the FRR, which can be easily constructed by connecting one input port and one output port of commercial 2×2 fiber coupler, as shown in Fig. 4 Step 2. The structure and principle of the FRR are described in Appendix A. In our experiments, the FRR used had a coupling ratio of 9:1 and was sensitive to external disturbances. The sensing region was then connected into the resonator. To mitigate potential interferences effects, Only a small portion of the ring resonator is exposed as the sensing region, eliminating potential interferences unrelated to the sensor's function. As shown in Fig. 4 Step 3, the ring resonator and coupler of the FRR are enclosed in a rigid protective shell to shield the resonator from interference caused by human or robotic interaction during braille recognition. Figure 4(b) presents photographs of the device captured during the sensor manufacturing process.

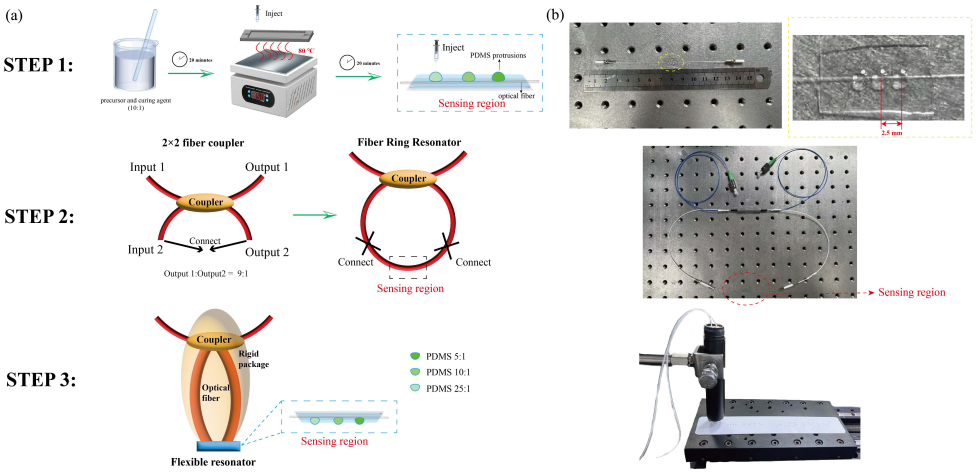

Fig. 4. (a) The schematic diagrams of the sensor fabrication process.(b) The corresponding images of the actual fabricated device of each step.

Optics EXPRESS

4.2. Characteristics analysis of braille sensor

The transmission spectrum of the FRR was characterized by scanning the tunable laser source across its resonance peak. This was achieved by driving the laser's piezoelectric transducer (PZT) with a triangular wave signal at a frequency of 10 Hz and a peak-to-peak voltage of 1 Vpp. To generate the PDH error signal, a narrow-linewidth tunable laser source was phase-modulated with a sinusoidal driving signal at a frequency of 900 kHz and a peak-to-peak voltage of 400 mVpp, which is lower slightly than the PD output power. The PD output signal was mixed with the reference signal that has the same frequency as the modulation signal. The phase of the reference signal is adjusted by a phase shifter to maximize the error signal. Then a fourth-order Butterworth low-pass filter was implemented to eliminate high-frequency components, enabling the acquisition of the PDH error signal. The PDH error signal is split into two branches. One branch of the PDH error signal is fed to a PI servo controller to form a closed loop, which generates a control signal for synchronizing the laser frequency to the cavity resonance frequency. The other branch is recorded by the oscilloscope as the sensor system output for further analysis. Figure 5(a,b) shows the transmission spectrum under modulation and its demodulation curve. Estimation through experimental data shows that the FRR has an extremely narrow full width at half maximum (FWHM) of 0.1 pm. The PDH error signal exhibits an excellent linearity of 31.65 V/pm near the resonance and has a wide dynamic range of 55 mV.

A manual force tester equipped with a digital force gauge (Handpi instruments HP-500) is used to provide external pressure in the experiment for testing the characterization of force sensing to provide external pressure. The voltage of the PD output increased slightly corresponding to the applied pressure because of resonance shift, while the peak voltage did not reach the maximum and then recovered to the minimum value as the closed-loop system worked. Three cylindrical PDMS protrusions were secured on the FRR to measure the responses of the FRR to static pressure. To achieve a gradient of hardness, The PDMS solution was fabricated by adjusting the weight ratios of precursor and curing agent in various mass ratios of 5:1, 10:1, and 20:1 to achieve different hardness of the protrusions after curing. These protrusions were then secured on the optical skin.

The experiment measured the pressure response of the sensor at three points within the range of 0–3 N, which aligns with the typical pressure exerted by a human finger when touching a braille character. Meanwhile, the system's output response remains within the optimal measurement range. Figure 5(c) shows the system's voltage shift recorded under different forces using PDMS protrusions with three hardness levels (ratios of 5:1, 15:1, and 25:1). Acting as probes, the PDMS protrusions compress against the sample surface, transferring the applied pressure to the optical fiber. The resonance frequency shift becomes more pronounced under identical pressing strokes when the sample is harder. Typically, the detection limit of the sensor is approximately 100 mN at a PDMS ratio of 10:1. Furthermore, linear fitting was performed in Fig. 5(d) to analyze the relationship between the voltage shift and the applied pressure for the three different hardness protrusions. The figure indicates that the system feedback voltage increased more under the same press force when the protrusion was harder, as more deformation was taken by the resonator. The slopes of the fitting curves are 0.058 N/mV, 0.071 N/mV, and 0.083 N/mV, respectively. Figure 5(e) shows the output voltage shift of the PDH error signal as the environmental temperature increases from 20°C to 35°C in 5°C increments. The overall fluctuation error of the test data is less than 1.5 mV, indicating a stable performance. As shown in Fig. 5(f), The PDH error signals exhibit an overall fluctuation error of less than 1.84 mV by alternatively changing the applied pressures from 1 N to 3 N for 20 circles. The standard deviations recorded were 0.67 mV, 0.48 mV, and 0.57 mV for applied pressures of 1 N, 2 N, and 3 N, respectively. The results show that the FRR sensor system exhibits excellent stability.

Furthermore, the stability of the sensor was tested under changing temperature conditions. The air conditioner was set to cooling mode with the temperature set at 23°C, and a thermometer

Optics EXPRESS

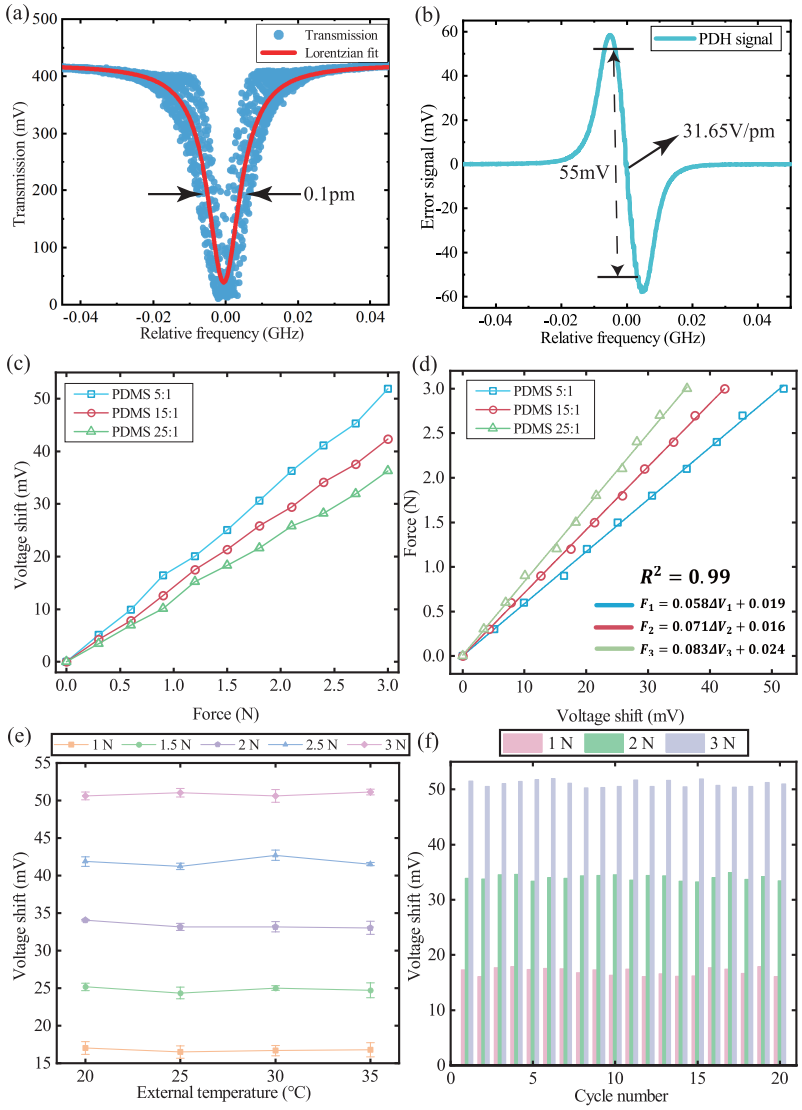

Fig. 5. (a,b) Transmission spectrum and demodulation curve of the tactile sensor system output.(c) Relationship between PDH error signal voltage variation and applied pressure curve. (d) Curve fitting relationship between applied pressure and voltage variation within the range of 0-3N. (e) The output of the sensor under different applied pressures (1-3 N) when external temperature changes. (f) The repeatability of the sensor is tested by alternately switching the applied pressure among 1N, 2N, and 3N.

was used to record temperature data at one-minute intervals. Figure 6(a) shows the process of change during temperature decreasing and recovering. Two time periods, each lasting 2 minutes, were selected for stability testing. The first period featured rapid temperature changes of 0.3°C/min during the decreasing phase, and the second period had a rate of 0.1°C/min during the recovery phase. The sensor was slid over the braille with different dots arrangements. Each dots arrangement was tested 5 times in total,and the difference between the highest and lowest output voltages was calculated. As shown in Fig. 6(b), the maximum voltage difference was 1.8 mV during the decreasing process, and 1.5 mV during the recovering process. The voltage

Optics EXPRESS

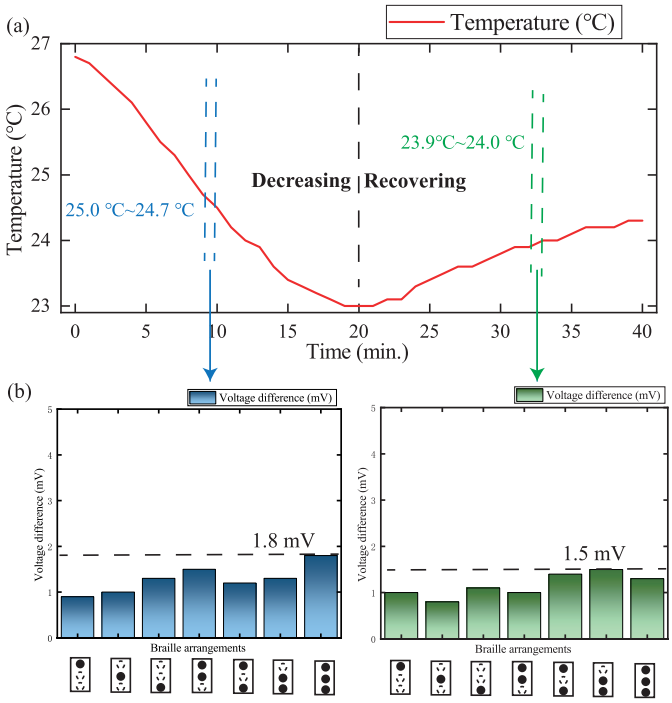

Fig. 6. (a) Temperature change curve. (b) Voltage differences for different braille arrangements as the sensor slides across the braille.

fluctuations remained within the controllable range and did not affect the experimental results. The results indicate that tiny fluctuation of room temperature will have a minor impact on the system output, but will not influence the recognition accuracy.

4.3. Intelligent braille recognition assisted by AI

Characters in braille are represented by a cell constructed of six raised dots that are arranged in three rows and two columns. The blind touch the braille with their fingers to perceive the arrangement of the braille dots on it. This process relies on the sense of touch. After knowing the arrangement of the braille dots, the blind can translate it into understandable language by comparing the braille and language (such as English) they have learned. Based on this method, a

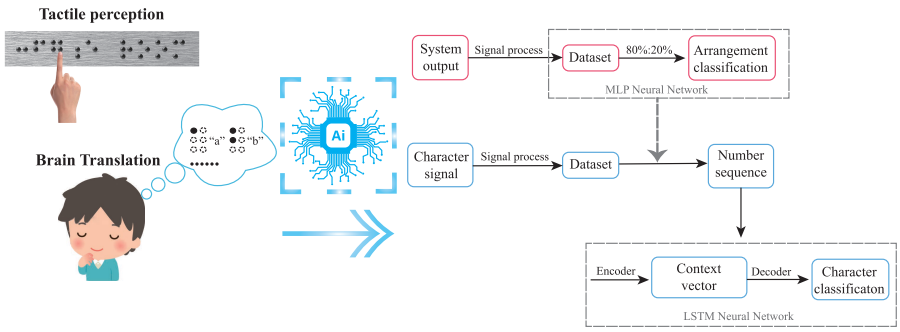

Fig. 7. The flowchart of the algorithm for braille recognition.

Optics EXPRESS

biomimetic sliding strategy is further proposed to achieve real-time and effective recognition of braille characters with the assistance of artificial intelligence (AI). As the sensor slides across the braille surface, different dot arrangements produce different amplitudes of pressure, with the signal of each character composed of two tactile pressures. The braille information is embedded within the time-series signals formed by the tactile pressures.

Figure 7 shows the process of intelligent braille recognition. The arrangement of three dots generates seven distinct pressure signals, along with a zero-pressure signal, so accurately distinguishing these different amplitudes of pressure signals is fundamental to recognizing braille information. When the sensor slides over the braille, the contact force is not always the same. Using a neural network, we can classify the output signals for different arrangements, allowing for small differences in contact force during the sliding process. To improve the recognition accuracy and system versatility, the braille bumps corresponding to arrangements and combinations of three points are tested with a Multilayer Perceptron (MLP) Neural Network [26,27]. The database is composed of tactile pressure signals produced by contact between the sensor and the braille board during the sliding process. It is divided into training and testing datasets according to a 4:1 ratio. Each signal is labeled with the corresponding dot arrangements and subsequently transformed into a tensor. These tensors are then input into a fully connected three-layer perceptron neural network, which is utilized to estimate the target dot arrangements. When the tactile pressure signal is input into the trained network, the dot arrangements can be read out. Furthermore, to achieve the classification and recognition of English words and sentences with contextually related features, a long short-term memory (LSTM) machine translation model was trained using 5 English words [28].

Figure 8(a) illustrates the tactile pressure signals associated with the recognition of braille representations of English characters. The signal comprises a sequence of tactile pressure inputs, facilitating the identification of individual braille characters. For each column of three dots, excluding the all-flat configuration, there are seven possible raised dot patterns. As the optical fiber slides over the braille, the varying dot positions create different pressure levels on the fiber. A neural network is used to distinguish the signals generated by these varying pressures. The confusion matrix in Fig. 8(b) left shows that the classification accuracy reaches

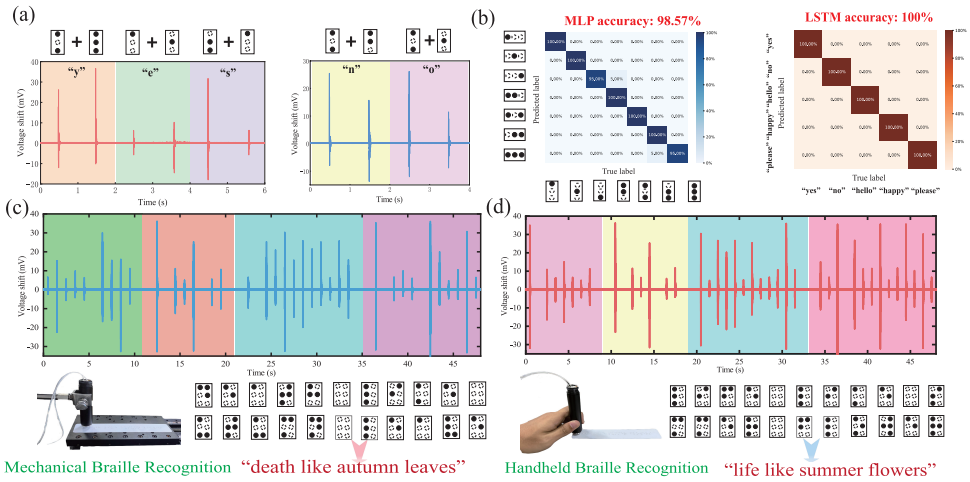

Fig. 8. (a) The signal feedback and display of recognition results of the braille characters on an oscilloscope. (b) Classification results of MLP and LSTM machine learning algorithms using confusion matrices. (c,d) braille recognition results in different braille sentences based on handheld and mechanical methods.

Optics EXPRESS

Table 1. Comparison of braille recognition using different sensors and machine learning algorithms

Ref.	Sensing mechanisms	Algorithm	Datasets	Accuracy
[11]	vision-based tactile sensor	YOLO v8	450 labelled real sharp images	87.5% at 315 wpm
[12]	piezoresistive sensor	Random Forests (RDFA)	26 English letters and common punctuation marks	99%
[14]	triboelectric nanogenerator-based tactile sensor	one-dimensional Convolution Neural Network (1D CNN)	11-digit phone numbers	96.12%
[29]	capacitive tactile sensor	Long Short-Term Memory (LSTM)	Braille letters from "A" to "Z" as well as "space"	97%
[13]	piezoelectric and piezoresistive dual-mode tactile sensor	CNN-LSTM neural network	20 kinds of braille	90.58% in double mode
[16]	FBG sensor	none	5 characters	none
[30]	FBG sensor	random forest and back propagation neural network	2 words	none
[15]	micro-nano optical fiber sensor	LSTM neural network	22 and 26 characters	98.58%(22 characters) and 97.10%(26 characters)
This work	optical fiber resonator sensor and PDH demodulation	MLP-LSTM model	7 dots arrangements and 5 English letters as well as poetry sentences	98.57% (dots) and 100%(letters and sentences)

98.57%. Furthermore, to better demonstrate the system's ability to process and interpret braille information, 5 English words were selected, and an LSTM neural network was applied to classify the time-series signals generated by these 5 words. Figure 8(b) right shows a classification accuracy of 100%, which means that even if there are slight errors in the recognition of each column, they do not affect the overall understanding of braille. As illustrated in the Fig. 8(b), even when the sensor introduces minor errors in classifying the pressure signals, the LSTM model effectively mitigates the impact of these errors during the translation of the digital sequence into English text. Based on the MLP-LSTM model, we hope to get an English sentence. It is significant to keep the contact force consistency between sensor and braille for the accuracy of the signal of the sensor. So, the sensor was fixed on an electric displacement stage to recognize braille sentences. Figure 8(c) shows the original signal of braille recognition, the transcoded sentence, and the actual pictures of the experimental process. The figure shows the displacement stage and the process of human using the packaged sensor to conduct actual experiments. Furthermore, to expand the application scenarios of the sensor, we conducted braille recognition experiments by carefully holding and sliding the sensor manually. Similarly, Fig. 8(d) show the process of recognition through handheld sensor.

Table 1 compares the accuracy of braille recognition using different sensors and machine-learning algorithms proposed by the authors. The basic principles of fiber optic sensors and electrical braille sensors, the auxiliary algorithms involved, and the final braille recognition accuracy are listed in the table. It can be seen that the FRR demodulated by the PDH technology

Optics EXPRESS

proposed in this study combined with machine learning has unique advantages in achieving accurate and fast braille recognition. The recognition accuracy is better than other sensor and algorithm combinations. By training the network with a wider range of words and sentences, full translation capabilities can be achieved without the need for individuals to laboriously learn braille rules.

5. Conclusion

In this study, the optical fiber tactile sensing system using a flexible FRR for braille recognition is proposed, in which the FRR is packaged using a PDMS solution with a 3D-printed mold to form a flexible optical skin. The PDH optical frequency locking technique is used to interrogate tactile pressure and convert frequency fluctuations into voltage shifts. The performance of the pressure response is illustrated by experiments: through theoretical analysis and optimization of the sensor and closed-loop system parameters, high precision, and fast measurements are enabled. The PDH demodulation curve exhibits a steep linear slope, enabling high sensitivity and high resolution of the sensing system. The system's linear region of the PDH error signal extends up to approximately 55 mV, which is responsive to tactile pressure ranging from 0 to 3 N. By adjusting the closed-loop PDH system parameters, the average response time to tactile pressure is reduced to less than 0.1s, meeting the requirements for fast dynamic response in braille reading. Furthermore, the sensing system is utilized for continuous braille character recognition by implementing a biomimetic sliding approach with the assistance of artificial intelligence. To achieve effective decoding of braille dot patterns through tactile pressure feedback, three small protrusions with different hardness are secured on the resonator to transfer different exerted pressures. Eight different arrangements composed of three dots are fully distinguished using a Multilayer Perceptron Neural Network, achieving a classification accuracy of 98.57%. Consequently, all braille information, including letters, numbers, and punctuation, can be interpreted as the sensor slides over the braille board. The LSTM neural network is applied to classify the time-series signals generated by 5 words, and the classification accuracy of 100% means that even if there are slight errors in the recognition of each column, it will not affect the transcoding of the braille. The fiber optic tactile sensing system uses the high-quality factor FRR and PDH demodulation method to achieve tactile pressure resolution of general braille dots, effectively distinguishing eight different braille arrangements. Then, with the assistance of machine learning algorithms, it achieves accurate transcoding of braille information, effectively overcoming the influence of error factors. The research of Bionic tactile sensor based on flexible optical FRR will further promote the advancement of tactile sensing techniques and intelligent braille recognition, potentially finding applications in the fields of smart medical care and intelligent robotics.

Appendix A: Principles of FRR and PDH method

The fundamental reflective FRR structure consists of three key components: a straight waveguide, a ring-shaped optical waveguide, and a directional coupler. As shown in Fig. 9, light is launched into the straight waveguide at port 1. Upon reaching the directional coupler, a portion of the light is coupled into the ring cavity via port 4, while the remaining light continues propagating through the straight waveguide and exits at port 3. The coupled light propagates around the ring and re-enters the coupler at port 2. Here, a second partial coupling occurs, directing a portion of the light back into the straight waveguide for output at port 3, with the remaining portion continuing to circulate within the ring cavity. The transmission characteristics of each port of the FRR can be analyzed using the transmission matrix.

Optics EXPRESS

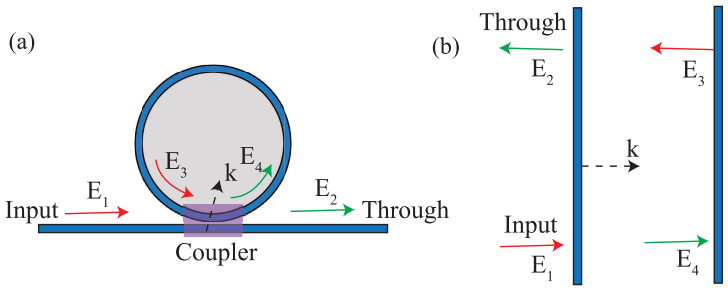

Fig. 9. Schematic diagram of fiber ring resonator (a) and equivalent FP cavity(b)

$$\begin{bmatrix} E_3 \\ E_4 \end{bmatrix} = \sqrt{1-\gamma} \begin{bmatrix} \sqrt{1-k} & j\sqrt{k} \\ j\sqrt{k} & \sqrt{1-k} \end{bmatrix} \begin{bmatrix} E_1 \\ E_2 \end{bmatrix} \tag{4}$$

$$E_2 = e^{-\alpha_L} e^{j\beta L} E_4$$

where, E_i $(i = 1, 2, 3, 4)$ respectively denotes each port of the FRR, γ is the insertion loss of the directional coupler, k is the power coupling coefficient of the directional coupler, α_L and βL is the transmission loss and the phase change respectively through the optical fiber. When the light satisfies the phase-matching condition:$\beta L = 2\pi$, after propagating one round trip within the ring cavity, it undergoes constructive interference with the light at the through port, leading to confinement within the cavity. FRR is a typical multi-beam interferometer and its transmission spectrum exhibits sharp absorption peaks the resonance condition can be concluded:

$$n_{eff} \frac{L}{\lambda} = q \tag{5}$$

where, n_{eff} is the effective refractive index of optical fiber, L is the length of the resonator, λ is the wavelength, and q is a positive integer.

The PD output signal comprises a superposition of harmonics arising from the modulation frequency. However, the signal of interest, containing the resonant cavity sensing information, is masked by these harmonic noises. Consequently, correlation detection techniques are employed to extract the desired signal. The lock-in amplifier (LIA) is a specific type of correlation detector, utilizing a multiplier and a low-pass filter to achieve this [31,32]. The detailed processes of the modulation and demodulation within a LIA are as follows.

The electric field of the incident light undergoes phase modulation and its electric field expression can be effectively expanded using the Jacobi-Anger expansion. When the modulation depth is small, the limited modulation depth confines the majority of the optical power within the carrier and the first-order sidebands. Consequently, the interaction with the resonator can be approximated as the simultaneous illumination by three distinct beams: the central carrier and

Optics EXPRESS

the two neighboring first-order sidebands.

$$\begin{aligned} E_{in} &= E_0 e^{j[2\pi(f_0+f_{PZT})t+M\sin 2\pi f_m t+\phi_0]} \\ &= E_0 e^{j[2\pi(f_0+f_{PZT})t+\phi_0]} \sum_{n=-1}^{+1} J_n(M) e^{j(n2\pi f_m t)} \\ &= E_0\{J_0(M)e^{j[2\pi(f_0+f_{PZT})t+\phi_0]} + J_1(M)e^{j[2\pi(f_0+f_{PZT}+f_m)t+\phi_0]} \\ &\quad + J_{-1}(M)e^{j[2\pi(f_0+f_{PZT}-f_m)t+\phi_0]}\} \end{aligned} \tag{6}$$

where, E_0 is the amplitude of the incident light, f_0 is the initial center output frequency of the laser, f_{PZT} is the speed of PZT frequency modulation, M is the modulation coefficient, which can be calculated by $M = \pi\frac{V_m}{V_\pi}$, V_m and f_m are depth and frequency respectively of phase modulation, V_π denote the half-wave voltage of the EOM, ϕ_0 is the initial phase.

It is the first harmonic signal of the modulation frequency that functions as the signal to be demodulated only remaining the DC term and the first harmonic signal, because they encapsulate the information of phase change of the resonator. The electric field of the emergent light is the superposition of each carrier component and can be expressed as:

$$\begin{aligned} E_{out} &= E_0\{h_0 J_0(M)e^{j[2\pi(f_0+f_{PZT})t+\phi_0]}e^{j\Phi_0} \\ &\quad + h_1 J_1(M)e^{j[2\pi(f_0+f_{PZT}+f_m)t+\phi_0]}e^{j\Phi_1} \\ &\quad + h_{-1} J_{-1}(M)e^{j[2\pi(f_0+f_{PZT}-f_m)t+\phi_0]}e^{j\Phi_{-1}}\} \end{aligned} \tag{7}$$

where, h_n and Φ_n represent the amplitude transfer coefficient and phase transfer coefficient respectively.

The PD output power contains intermodulation products arising from the mixing of three waves with distinct frequencies. We are particularly interested in the terms generated by the interference between the carrier and the first-order sidebands, as these terms encode phase demodulation information crucial for resonator characterization. A lock-in amplifier is employed to demodulate the desired signal from the complex PD output. This instrument, consisting of a multiplier, a LPF, and a phase shifter, offers a robust technique for extracting weak signals buried in noise. The PD output is first multiplied by a reference signal within the multiplier. Subsequently, the LPF removes high-frequency components, resulting in a DC output that is in phase with the frequency shift signal of the resonator. By adjusting the phase of the reference signal using the phase shifter, the lock-in amplifier output can be maximized, enhancing the signal-to-noise ratio and facilitating accurate demodulation. The output signal of the LIA can be summarized as:

$$V_{fil} = R_{pd} I_0 (A_1 \sin\theta - B_1 \cos\theta) \tag{8}$$

Near the resonance frequency, the response curve exhibits near-linearity. This characteristic allows the slope of this linear region to be effectively captured by the zero-point slope:

$$k_0 = \left.\frac{dV_{fil}}{d\Delta f}\right|_{\Delta f=0} \tag{9}$$

where Δf is the frequency offset between the laser and the resonator.

Appendix B: MLP neural network and LSTM model

The output value of the neuron in the neural network can be expressed by the following equation:

$$y = max(0, \omega^T X + b) \tag{10}$$

where X is the input value, ω^T and b are weights and biases respectively.

Optics EXPRESS

The network parameters are updated using the backpropagation algorithm, resulting in the formation of the MLP neural network. This network establishes a nonlinear mapping between the input tactile signals and the output target dot arrangements. The output value of the neuron in the LSTM can be expressed by the following equation:

$$h_t = O_t tanh(f_t C_{t-1} + i_t C_t) \tag{11}$$

where f_t, i_t, and O_t represent the forget gate, input gate and output gate of the LSTM model. The update of the neural network parameters can be expressed using the following equation:

$$\begin{aligned} \omega_{new} &= \omega_{old} - \eta \nabla E(\omega) \\ b_{new} &= b_{old} - \eta \nabla E(b) \end{aligned} \tag{12}$$

where η is the learning rate, ∇ represents the gradient operator.

Funding. National Key Research and Development Program of China (2022YFE0140400); National Natural Science Foundation of China (62405027); Scientific Research Project of Liaoning Provincial Education Department (LJKMZ 20220544).

Disclosures. The authors declare no conflicts of interest.

Data availability. Data underlying the results presented in this paper are not publicly available at this time but may be obtained from the authors upon reasonable request.

References

1. J. Wang, X. Liu, R. Li, *et al.*, "Biomimetic strategies and technologies for artificial tactile sensory systems," Trends Biotechnol. **41**(7), 951–964 (2023).
2. Y. Li, M. Zhao, and Y. Yan et al., "Multifunctional biomimetic tactile system via a stick-slip sensing strategy for human–machine interactions," npj Flexible Electron. **6**(1), 46 (2022).
3. T. Kim, I. Hong, and M. Kim et al., "Ultra-stable and tough bioinspired crack-based tactile sensor for small legged robots," npj Flexible Electron. **7**(1), 22 (2023).
4. A. L. Trejos, J. Jayender, and M. Perri et al., "Robot-assisted tactile sensing for minimally invasive tumor localization," The International Journal of Robotics Research **28**(9), 1118–1133 (2009).
5. S. Li, X. Chen, and X. Li et al., "Bioinspired robot skin with mechanically gated electron channels for sliding tactile perception," Sci. Adv. **8**(48), eade0720 (2022).
6. H. Oh, G.-C. Yi, M. Yip, *et al.*, "Scalable tactile sensor arrays on flexible substrates with high spatiotemporal resolution enabling slip and grip for closed-loop robotics," Sci. Adv. **6**(46), eabd7795 (2020).
7. N. Bai, Y. Xue, and S. Chen et al., "A robotic sensory system with high spatiotemporal resolution for texture recognition," Nat. Commun. **14**(1), 7121 (2023).
8. Y. Yan, Z. Hu, and Z. Yang et al., "Soft magnetic skin for super-resolution tactile sensing with force self-decoupling," Sci. Robot. **6**(51), eabc8801 (2021).
9. S. Isayed and R. Tahboub, "A review of optical braille recognition," in *2015 2nd World Symposium on Web Applications and Networking (WSWAN)*, (IEEE, 2015), pp. 1–6.
10. B.-S. Park, S.-M. Im, and H. Lee et al., "Visual and tactile perception techniques for braille recognition," Micro and Nano Syst Lett **11**(1), 23 (2023).
11. P. Potdar, D. Hardman, E. Almanzor, *et al.*, "High-speed tactile braille reading via biomimetic sliding interactions," IEEE Robot. Autom. Practice **1**, 1 (2024).
12. X.-F. Zhao, C.-Z. Hang, and H.-L. Lu et al., "A skin-like sensor for intelligent braille recognition," Nano Energy **68**, 104346 (2020).
13. Z. Gao, L. Chang, and B. Ren et al., "Enhanced braille recognition based on piezoresistive and piezoelectric dual-mode tactile sensors," Sens. Actuators, A **366**, 115000 (2024).
14. Y. Lu, D. Kong, and G. Yang et al., "Machine learning-enabled tactile sensor design for dynamic touch decoding," Adv. Sci. **10**(32), 2303949 (2023).
15. L. Huang, B. Luo, and X. Zou et al., "Research on efficient braille recognition based on the pair-u-shaped micro-nano optical fiber fingerprint-like tactile sensors," Optics Laser Technology **179**, 111349 (2024).
16. A. Prasad, S. Sebastian, and S. Asokan, "Diaphragm-micro-stylus-based fiber bragg grating tactile sensor," IEEE Sens. J. **20**(12), 6394–6399 (2020).
17. N. Yao, X. Wang, and S. Ma et al., "Single optical microfiber enabled tactile sensor for simultaneous temperature and pressure measurement," Photonics Res. **10**(9), 2040–2046 (2022).
18. Z. Wang, Z. Chen, and L. Ma et al., "Optical microfiber intelligent sensor: wearable cardiorespiratory and behavior monitoring with a flexible wave-shaped polymer optical microfiber," ACS Appl. Mater. Interfaces **16**(7), 8333–8345 (2024).

Optics EXPRESS

19. K. Xiao, Z. Wang, and Y. Ye et al., "Pdms-embedded wearable fbg sensors for gesture recognition and communication assistance," Biomed. Opt. Express **15**(3), 1892–1909 (2024).
20. X. Zhan, Z. Wang, and S. Kumar et al., "The application of pound-drever-hall technology in high resolution sensing-a review," IEEE Sens. J. **23**(7), 6427–6438 (2023).
21. Q. Liu, S. Zhao, and Z. He, "Improved pound-drever-hall techniques for high resolution optical fiber grating sensors," J. Lightwave Technol. **39**(12), 3846–3854 (2021).
22. X. Ma, Z. Cai, and C. Zhuang et al., "Integrated microcavity electric field sensors using pound-drever-hall detection," Nat. Commun. **15**(1), 1386 (2024).
23. Y.-S. Jang, J. Lim, and W. Wang et al., "Measurement of sub-fm/hz 1/2 displacement spectral densities in ultrahigh-q single-crystal microcavities with hertz-level lasers," Photonics Res. **10**(5), 1202–1209 (2022).
24. B. Culshaw and A. Kersey, "Fiber-optic sensing: A historical perspective," J. Lightwave Technol. **26**(9), 1064–1078 (2008).
25. K. J. Vahala, "Optical microcavities," Nature **424**(6950), 839–846 (2003).
26. L. Chen, S. Karilanova, and S. Chaki et al., "Spike timing–based coding in neuromimetic tactile system enables dynamic object classification," Science **384**(6696), 660–665 (2024).
27. B. Shih, D. Shah, and J. Li et al., "Electronic skins and machine learning for intelligent soft robots," Sci. Robot. **5**(41), eaaz9239 (2020).
28. I. Sutskever, O. Vinyals, and Q. V. Le, "Sequence to sequence learning with neural networks," Advances in neural information processing systems **27**, 1 (2014).
29. S. F. Müller-Cleve, V. Fra, and L. Khacef et al., "Braille letter reading: A benchmark for spatio-temporal pattern recognition on neuromorphic hardware," Front. Neurosci. **16**, 951164 (2022).
30. T. Li, A. Zhang, and M. Du et al., "A fingertip optical fiber composite sensor with conformal design for robotic perception of tactile force," IEEE/ASME Transactions on Mechatronics **1**, 1 (2024).
31. E. D. Black, "An introduction to pound–drever–hall laser frequency stabilization," Am. J. Phys. **69**(1), 79–87 (2001).
32. W. Liang, V. S. Ilchenko, and A. A. Savchenkov et al., "Resonant microphotonic gyroscope," Optica **4**(1), 114–117 (2017).